Exploring wetting dynamics of water nanodroplet on nano-textured surfaces: atomistic insights

Ilemona S Omeje, Djafar Iabbaden, Patrick Ganster, Tatiana Itina

Exploring wetting dynamics of water nanodroplet on nano-textured surfaces: atomistic insights

Ilemona S. Omeje*[1], Djafar Iabbaden[2], Patrick Ganster[3], and Tatiana E. Itina[1]

[1] *Université Jean Monnet, CNRS, Institut d'Optique Graduate School, Laboratoire Hubert Curien, Saint-Etienne, France*

[2] *LEM3, CNRS – Université de Lorraine – Arts et Métiers ParisTech, 7 rue Félix Savart, 57070 Metz, France*

[3] *Mines Saint-Étienne, Univ. Lyon, CNRS, UMR 5307 LGF, Centre SMS, F - 42023 Saint-Étienne, France*

Abstract

The static and dynamic wetting behaviors of a water nanodroplet are investigated on flat and structured titanium (Ti) surfaces by using a fully atomistic simulation. Firstly, the results obtained for a water nanodroplet on a flat Ti surface agree with the static contact angle reported in the literature. Furthermore, to unveil the mechanisms of the water nanodroplet behavior on nano-textured surfaces, we analyze the impact of the roughness factors, the structure period, and sizes compared to the nanodroplet diameter. The introduction of the surface roughness produces an inhomogeneous spreading of the nanodroplet. The degree of roughness and the specific dimensions of the surface grooves determine these wetting processes. Surfaces with larger grooves and spacing tend to support more extensive spreading, while those with narrower grooves and higher roughness limit spreading. The obtained results also demonstrate damping in droplet vibrations accompanied by a gradual decrease in the dynamic contact angle of water nanodroplets on both flat and rough Ti surfaces, indicating a transition to a hydrophobic state. This effect is caused by the atomic bonding of water atoms to the surface ones and is shown to strongly depend on the surface roughness factors. The simulation results provide atomic-level insights into the wetting mechanisms on surfaces featuring nanometric and sub-micrometric roughness, typically induced by femtosecond laser processing.

Keywords: wetting, contact angle, titanium, femtosecond laser, roughness, molecular dynamics, nanodroplet

1 Introduction

Ti and its alloys are highly promising materials, especially for biomedical applications due to their biocompatibility, high strength, and fracture toughness [1]. These characteristics make them ideal for dental and orthopedic implants. It is well known that one of the most effective ways to improve Ti bone integration with these implants is by introducing appropriate surface roughness [2]. Surface texturing may also improve its antibacterial properties. Among several methods of surface treatment, femtosecond laser processing has notable advantages. These include high processing resolution and a minimal heat-affected zone [3]. Additionally, this method allows one to fabricate complex 2D and 3D structures [4, 5]. In this context, adjusting the wettability of the surface plays a fundamental role, as it dictates how the implant interacts with surrounding tissues and promotes the cell attachment to prevent bacterial growth [2, 6]. Therefore, a deep understanding of these wetting properties is very important.

Several models have been developed to account for surface topography and heterogeneities, taking into account chemical patterns and impurities on the textured surfaces [7]. For surfaces treated with femtosecond lasers, the experimentally observed apparent contact angle (CA) often differs from the predictions of Young's model [8–11]. This discrepancy is theoretically explained by using the Wenzel and Cassie-Baxter equations that account for these surface irregularities [12, 13]. The Wenzel model assumes that the liquid fully penetrates the solid's roughness and fills the gaps establishing a microscopic contact angle [12]. In contrast, the Cassie-Baxter model suggests that the liquid does not infiltrate the grooves. Instead, a significant portion of the liquid-gas interface is pinned to the surface due to air entrapment [13].

These models have been consistently used within the laser community to quantify the wettability of laser-treated surfaces [14]. The Wenzel and Cassie-Baxter equations are typically applied to homogeneous and isotropic surfaces where the nanodroplet size to roughness scale ratio is large. However, it is well known that micro/nanostructures created with femtosecond lasers can exhibit heterogeneity [15]. Such heterogeneous topography can complicate the application of these models.

In addition, the nature of nano-surface processing and the challenges of conducting experiments at the nanoscopic scale remain challenging. These challenges restrict the capacity to improve our understanding of

*Corresponding author: ilemona.sunday.omeje@univ-st-etienne.fr

the interactions between nanodroplets and these specially textured surfaces. Therefore, Molecular Dynamics (MD) simulations are adequate to investigate the nanodroplet wetting properties on nanometer surface relief as reported in previous studies [16–18]. This approach is interesting because it allows for an easy assessment of the total energy resulting from interactions between atoms in a system. It also allows us to study droplet stability and its dynamic behavior.

Several studies were already focused on understanding the wettability of titanium dioxide (TiO_2) using atomistic approaches. For example, Park and Aluru [16] used MD simulations to show that the wettability of a TiO_2 surface increases with rising temperature due to a decrease in hydrogen bonding and surface tension. Similarly, Ohler and Langel [17] proposed a new model for the CA of water on TiO_2 surfaces using MD simulations. They argue that the macroscopic CA is not determined by the direct interaction of bulk water with the TiO_2 surface but rather by an interface between a thin, ordered layer of water molecules on the surface and the bulk water droplet.

Recently, Zhu et al. [18] investigated the wettability of three different phases of TiO_2 thin films: anatase, brookite, and rutile. The study found that the wettability of the TiO_2 surface depends on the crystal phase, with anatase being the most wettable (CA of 43.7°) and rutile the least wettable (CA of 73.9°). The authors attribute this difference to variations in the structural connection and arrangement of surface microtopography among the three phases. The study also found that increasing the roughness of the anatase surface decreases its wettability, further highlighting the role of surface morphology in determining wettability.

To the best of our knowledge, the wettability of Ti has not been extensively studied using MD simulations. Given the insights gained from MD studies on TiO_2, a similar atomistic approach to studying Ti wettability could provide a molecular-level understanding of the fundamental interactions, which can offer new perspectives and potentially lead to increased control over surface properties for various applications. In our recent study using hydrodynamic simulation, we demonstrated that to achieve more hydrophobic behavior on laser-textured surfaces, more attention should be paid to the height of the relief, and caution should be exercised when varying the period of the relief during femtosecond laser processing [19, 20].

In this study, MD is used to investigate the wettability of a water nanodroplet on flat and rough Ti surfaces similar to that of the rippled metasurfaces commonly made by femtosecond laser with structure sizes of a few tens of nanometers. Static and dynamic wetting phenomena are both examined by covering flat and structured surfaces. Furthermore, we measured both the static of water nanodroplets and compared to the prediction of classical wetting models discussed above. By comparing these results with experimental data and the classical wetting models, we provide deep insights into the mechanisms at play allowing us a better understanding of the wettability of the structured Ti surfaces.

Pair	σ **(nm)**	ε **(kJ/mol)**	**Charge (e)**
$O-O$	0.3166	0.1554	-0.8476
$H-H$	0.0	0.0	+0.4238
$Ti-Ti$	0.2718	0.8582	0
$Ti-O$	0.2942	0.3652	0

Table 1: SPC/E water and Ti force field interaction parameters values.

2 Simulations model and details

The water nanodroplet on the Ti surface is modeled using the Extended Simple Point Charge (SPC/E) model to represent liquid water [21]. The SPC/E model is a three-site rigid model with point charges on Oxygen (O) and Hydrogen (H) (Table 1). This model have been extensively used in wetting studies [22]. In this model, the interactions between water molecules are described using a combination of short-range Lennard-Jones (LJ) and long-range electrostatic potential energy, as given by the following equation:

$$\begin{aligned} U(r_{ij}) &= U_{non-bond}(r_{ij}) + U_e(r_{ij}) \\ &= 4\varepsilon_{ij}\left[\left(\frac{\sigma_{ij}}{r_{ij}}\right)^{12} - \left(\frac{\sigma_{ij}}{r_{ij}}\right)^{6}\right] \\ &\quad + \frac{1}{4\pi\epsilon}\sum_{i=1}^{3}\sum_{j=1}^{3}\frac{q_i q_j}{r_{ij}} \end{aligned} \tag{1}$$

The short-range LJ potential ($U_{non-bond}(r_{ij})$) represents the Van der Waal force between two non-bonding atoms. As shown in Equ. 1, it is defined by a conventional 12-6 function such that r_{ij} is the distance between the two atoms i and j, σ_{ij} is the distance at which the interaction energy between two atoms is minimal, and ε_{ij} is the depth of the potential well. In the Coulombic term ($U_e(r_{ij})$), ϵ represents the permittivity in vacuum, q_i and q_j denote the charges of the interaction sites. The OH bond length is 1 Å and the angle between H-O-H is fixed at 109.47°. To make the water molecule more rigid during the MD simulation, the SHAKE algorithm was used to constrain bond length and angle [23]. Long-range electrostatic interactions were computed using the Particle-Particle Particle-Mesh (PPPM) method [24]. The PPPM is more efficient than the Ewald method [25] because it can handle long-range interactions for periodic systems [26]. Non-bonding interactions, including both Van der Waals and electrostatic forces, were truncated at a cut-off distance of 12 Å. The interactions between Ti and O atoms were modeled using the 12-6 LJ potential, with parameters determined by the Lorentz-Berthelot mixing rule [27], as shown in Equ. 2.

$$\sigma_{ls} = \frac{\sigma_i + \sigma_j}{2}; \quad \varepsilon_{ls} = \sqrt{\varepsilon_i \cdot \varepsilon_j} \tag{2}$$

It should be noted that the interactions between Ti and H atoms are neglected in this study. This simplification based on the omission of LJ parameters for H atoms in the SPC/E water model is a well-established practice supported by extensive research and literature. The primary reasons for this simplification are computational efficiency and the focus to accurately capture the critical electrostatic interactions that determine the behavior of the water molecules [28, 29]. Additionally, because the bonds in the SPCE model of water are rigid, the H atoms are restricted from freely rotating and forming independent interactions with Ti [21]. Therefore, the H atoms are primarily involved in H bonding with neighboring water molecules [28], further reducing their availability for direct interaction with Ti. It is worth mentioning that neglecting H-substrate interaction may underestimate the influence of wetting behavior on highly reactive (laser-treated) surfaces that can readily form H bonds with the H atoms of water.

Surface (Surf)	h (nm)	w (nm)	s (nm)	p (nm)
Surf-1	0	0	0	0
Surf-2	0.28	0.911	1.109	2.02
Surf-3	0.28	0.509	0.511	1.02
Surf-4	0.78	1.011	1.009	2.02
Surf-5	0.78	0.509	0.511	1.02

Table 2: Values of the adjustable dimensional parameters such as height (h), width (w), spacing (s) and periodicity (p) of fence-like Ti nanostructures.

In addition, Ti-Ti interactions were calculated using the LJ potential. The LJ potential parameters for Ti interactions used in this study are modified in such a way that they can replicate the physical properties of Ti. The parameters have been validated against Density Functional Theory (DFT) calculations and experimental data. These parameters accurately reproduce the lattice constant and independent elastic constants, as detailed in the Supporting Information (1.1). The LJ potential parameter values used in the MD simulations of this study are provided in Table 1.

The nanodroplet corresponds to a sphere with a radius of 3.0 nm and contains 3009 water molecules. Previous studies have consistently demonstrated that droplets comprising 2000 atoms (or more) consistently produce reliable results [30]. Temperature equilibration of the nanodroplet and the Ti substrate was performed separately. The nanodroplet was equilibrated using a time step of 1 fs at 300 K for approximately 1 ns in the NVT ensemble. This duration was sufficient to achieve a stable nanodroplet configuration. To validate this configuration, the radial distribution functions (g(r)) obtained from our simulations were compared with the experimental data [31] and the SPC/E model [21], as shown in Fig. 1. The comparison indicates good agreement between our study, the experimental data, and the SPC/E model with slight deviations observed below the peaks of g(r). This agreement demonstrates that the SPC/E water model used in our MD simulations is appropriate and reliable.

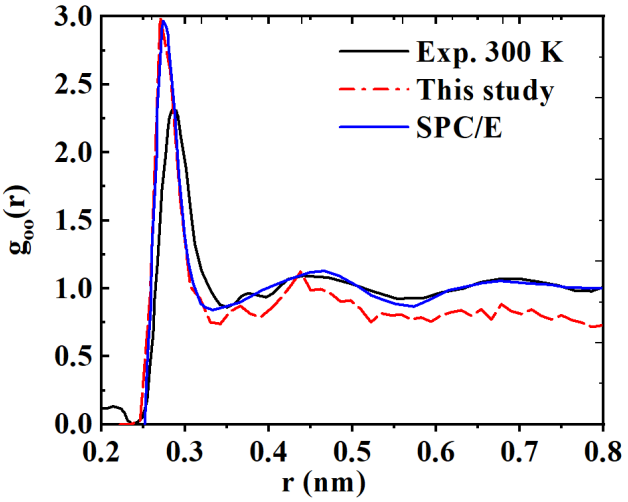

Figure 1: Radial distribution functions (g(r)) of oxygen-oxygen distances for real water [31], this MD study and SPC/E water model [21] at 300 K.

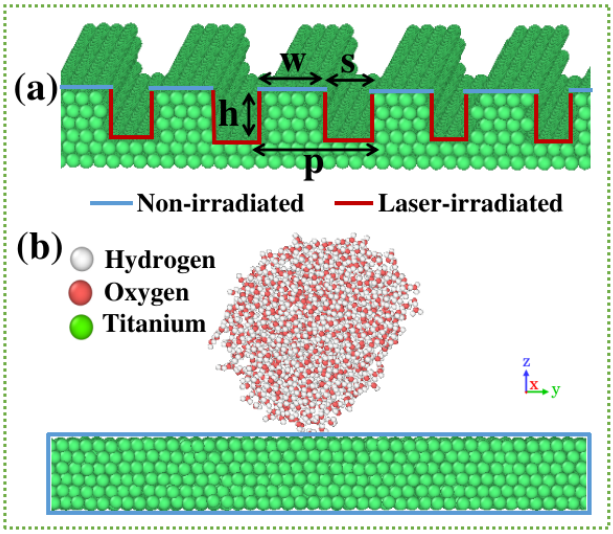

Figure 2: (a) A fence-like nanostructure on Ti surface with heights (h), widths (w), spacing (s), and the periodicity (p). (b) Initial atomistic configuration of water nanodroplet on the flat Ti surface.

The flat Ti substrate corresponds to a block of dimension 14.5 × 19.5 × 1.4 nm^3 containing 22344 atoms arranged in a Hexagonal Close-Packed (HCP) structure along [0-110] [10-10] [0001] directions. Subsequently, a nanometric pattern similar to laser-textured ones, having heights (h), widths (w), spacing (s), and a periodicity (p) as depicted in Fig. 2 (a), was introduced on Ti surfaces [20, 32, 33]. In our previous studies, it has been established that the structural parameters h, w, s, and p are adjustable based on the topography profile of the laser-patterned surfaces [20]. The adjustable parameters used in the wetting studies are summarised in Table 2. For the sack of clarity

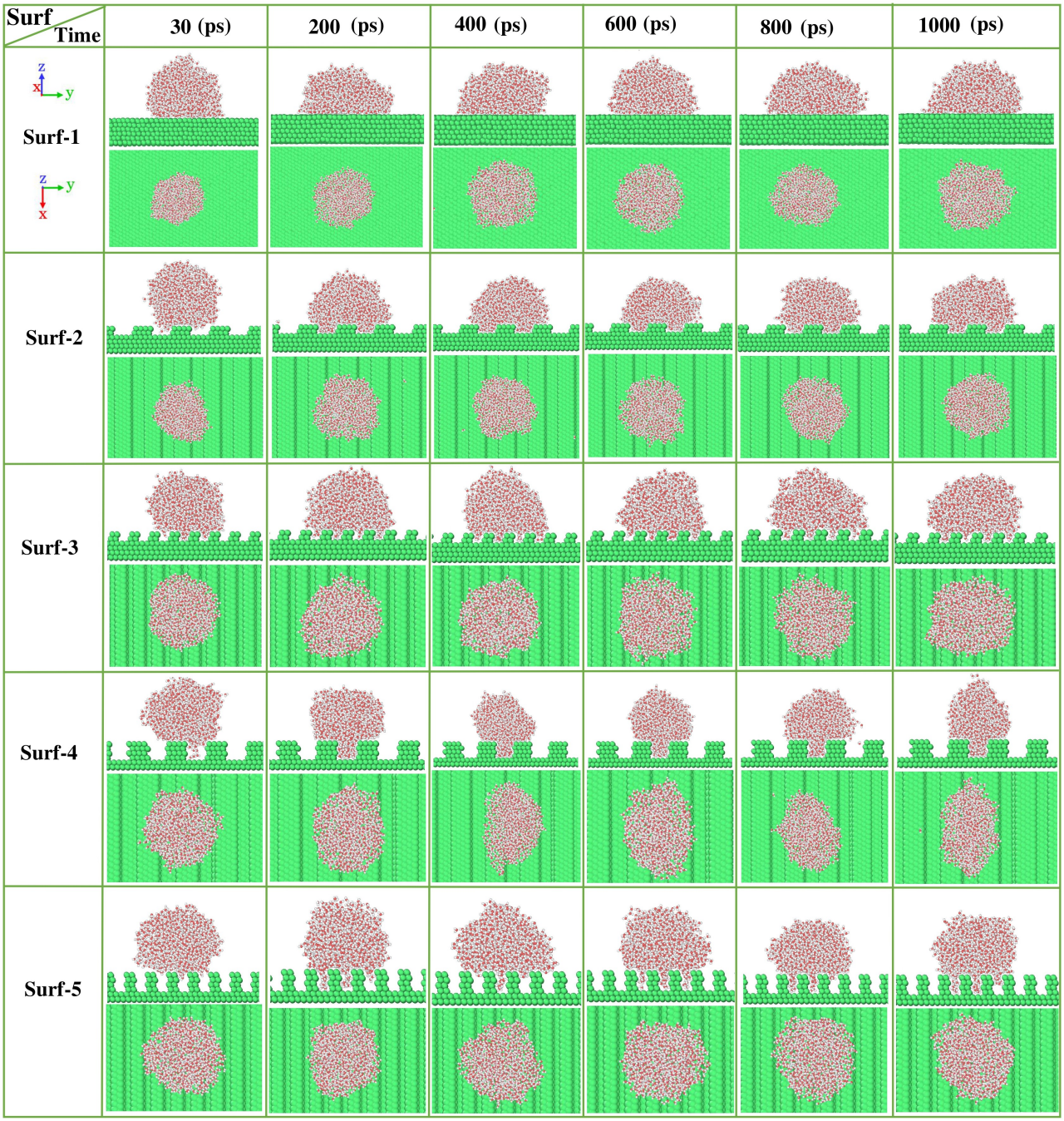

Figure 3: Snapshots of the side and front views of the spreading process of a water nanodroplet on Ti surfaces with different roughness scales as a function of time.

and to facilitate the adjustment of these parameters, we use the roughness factor (r) and fractional area (f) to quantify them, as shown in Equ. 3 below.

$$r = 1 + \frac{2h}{p}; p = w + s; f = \frac{w}{p} \tag{3}$$

The bulk Ti substrate was equilibrated using the NVT ensemble at 300 K for 1 ns with a time step of 1 fs. In addition, the equilibrated spherical nanodroplet was positioned on the equilibrated Ti surface, as shown in Fig. 2 (b). In this study, the flat and rough Ti substrates were completely frozen during the MD simulation. The fixed substrate in MD simulations, particularly in wetting studies, is a well-documented practice aimed at a reduced computational cost [28], maintaining numerical stability [34] and ensuring an accurate representation of the physical system [35, 36]. Interestingly, simulations with a fixed surface compared to a flexible surface have shown a negligible effect on the CA [22]. In addition to the simulation set-up, the size of the simulation box was set to 14.5 × 19.5 × 15.4 nm^3. Periodic boundary conditions were applied in the x, y, and z directions during the simulation of the water nanodroplet on the Ti surfaces. The entire simulation was carried out for 1 ns in the NVT ensemble with a time step of 1 fs. MD calculations were performed using the Large-scale Atomic/Molecular Massively Parallel Simulator (LAMMPS) software [37]. Visualization

and analysis of the water nanodroplet on Ti surfaces were conducted using OVITO software [38].

3 Results and discussion

In this section, we present the results of MD simulations of the model described above to investigate the wettability properties of both flat and nanorough Ti surfaces. Initially, we focused on the dynamic wetting behavior on both Ti surfaces by analyzing the spreading radius and dynamic CA of a nanodroplet. These analyses enabled us to determine the equilibrium state of the nanodroplet on the Ti surface. Subsequently, we studied the wettability of nanodroplets on rough Ti surfaces by evaluating the static CA and the influence of surface nanoroughness on the wetting properties. The results obtained were compared to existing classical wetting models such as the Wenzel and the Cassie-Baxter model.

3.1 Dynamic wetting behavior of Ti surfaces

To understand the fundamental process of nanodroplet spreading on the flat and nanometric Ti surfaces, the dynamics of the nanodroplet on the corresponding surfaces are examined. Thus, Fig. 3 shows the snapshots of the side and front views of the spreading process of a water nanodroplet on Ti surfaces with different roughness scales as a function of time.. The droplet on the flat surface (Surf-1) is initially spherical at 0 ps, indicating minimal spreading. Between 30 and 50 ps, the droplet starts to spread gradually, with a noticeable decrease in height. From 200 to 1000 ps, further spreading occurs, and the droplet becomes more stable with a large base and minimal height.

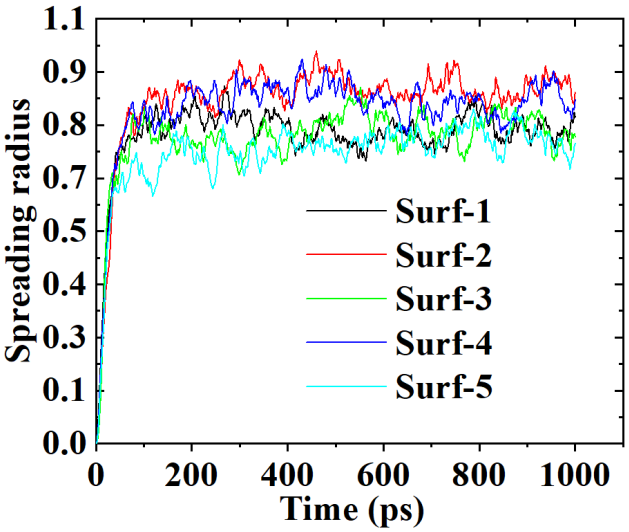

Figure 4: Normalized spreading radius of water nanodroplet on Ti surfaces with different roughness.

In the case of Surf-2, the droplet spreads and begins to interact with the rough surface by 30 ps. As time progresses, between 200 and 1000 ps, the droplet flattens out, forming a wide base that settles into the roughness grooves. This indicates a substantial degree of spreading. In contrast, for Surf-3, the spreading process is restricted by the roughness grooves. The droplet conforms to these grooves rather than spreading freely. This limitation occurs because Surf-3 has a greater number of grooves beneath the droplet compared to Surf-2. The equal distribution of w and s for Surf-3, as opposed to Surf-2, provides evidence for this increased groove density.

In Surf-4, the droplet spreads more extensively than in previous cases. Initially, from 30 to 200 ps, the droplet expands equally in both the x and y directions, filling one of the roughness grooves. This notable difference in spreading behavior can be attributed to the larger dimensions of the grooves in Surf-4, specifically the h, w, and s, as shown in Table 2. While the groove width and spacing in Surf-4 are similar to those in Surf-2, the grooves are deeper (greater h) in Surf-4. By 1000 ps, the droplet's base shrinks along the y-direction leading to a noticeable increase in the droplet's height along this axis while it continues to spread along the x-direction. However, for Surf-5, the droplet partially retracts, forming a ball-like shape with air pockets trapped beneath its surface. This altered spreading pattern is due to the significantly deeper grooves (higher h) in Surf-5, coupled with narrower w and s compared to Surf-2,3 and 4.

It is therefore important to state that the degree of roughness and the specific dimensions of the surface grooves (h, w, s and p) critically determine the wetting process. Surfaces with larger grooves and spacing (like Surf-2 and Surf-4) tend to support more extensive spreading, while those with narrower grooves and higher roughness (like Surf-3 and Surf-5) limit spreading.

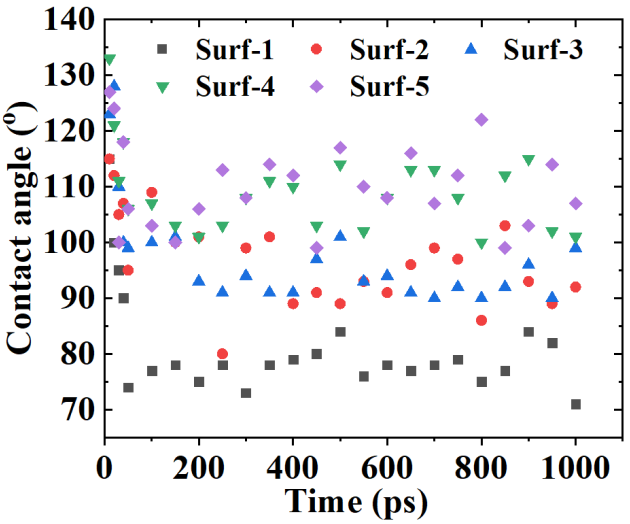

Figure 5: Dynamic contact angles of water nanodroplet at different times on Ti surfaces with different roughness scales.

Fig. 4 presents the normalized spreading radius as a function of time for water nanodroplets on Ti surfaces with varying roughness scales. Initially, the spreading radius increases rapidly, indicating that the droplets

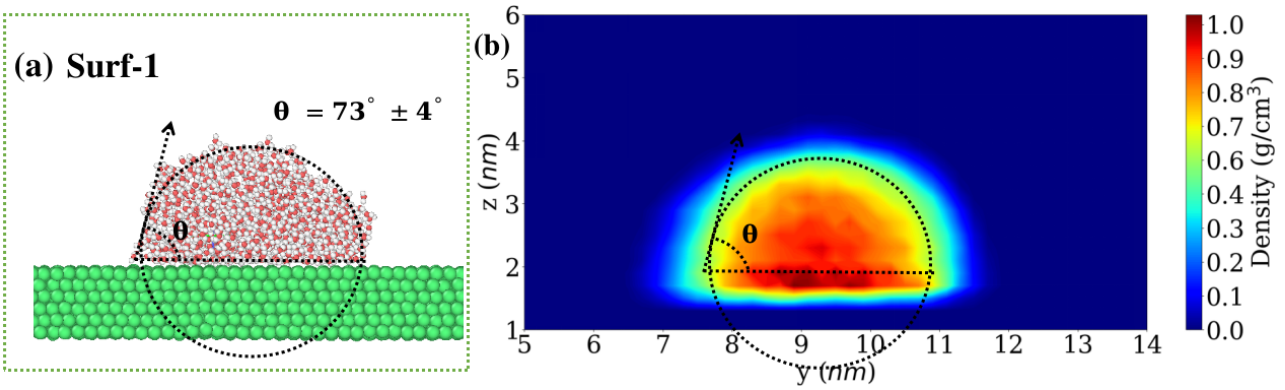

Figure 6: Measurement of static water contact angle: (a) snapshot of a water nanodroplet and (b) its density profile on a flat Ti surface with an indication of the water contact angle. In the density profile color bar, 1 corresponds to the liquid and 0 corresponds to the vapor.

begin to spread quickly upon contact with the surface. During the first 50 ps, there is a significant increase in the spreading radius for all surfaces. Beyond 50 ps, the spreading radius begins to approach a steady state.

It is observed that Surf-5 has the lowest spreading radius, followed by Surf-3. These observations validate the earlier claim about the similar roughness features of the two surfaces. Surf-2 has the highest spreading radius, followed by Surf-4. This further validates the results mentioned above concerning the two surfaces. The spreading radius of the flat surface (Surf-1) is lower than that of Surf-2 and 4 but higher than that of Surf-3 and 5. While the increased roughness in Surf-3 and 5 limits spreading, the spreading radius of Surf-2 and 4 is higher than that of Surf-1 because, as the droplet stabilizes, the droplet base on Surf-2 and 4 is larger compared to Surf-1.

Fig. 5 illustrates the dynamic CA of water nanodroplets as a function of time for Ti surfaces with varying roughness levels. At 30 ps, the CAs are generally high, indicating that the droplets initially exhibit minimal spreading on all surfaces. The initial CAs vary significantly with the roughness of the surfaces; for instance, Surf-1 starts at approximately 115°, whereas Surf-4 begins at around 133°. As time progresses, the CAs decrease, signifying that the droplets spread out on the surfaces. This decrease is most rapid during the initial 50 ps, reflecting the dynamic wetting process. Beyond 50 ps, the rate of decrease in CA slows down as the system approaches equilibrium, and the contact angles stabilize. Notably, Surf-5 exhibits a higher CA compared to Surf-4, 3, 2, and 1. This behavior indicates that rougher surfaces, such as Surf-5, prevent wetting more effectively than smoother ones, leading to higher CA. The higher roughness in Surf-5 makes it trap air pockets under the droplet, reducing the actual contact area between the droplet and the surface.

Thus, in general, the CA increases as roughness rises shifting the wettability of Ti surfaces from hydrophilic (Surf-1) to hydrophobic state for other surfaces. These observations for Surf-2, 3, and 4 align with the main assumption of the Wenzel model. The Cassie-Baxter model somewhat better describes Surf-5, where air pockets exist between the droplet and the rough Ti surface, generally leading to higher CAs and less wetting. Interestingly, despite small sizes, the initial rapid decrease in CA and an increase in spreading radius is similar to the dynamic wetting theories and previous simulation studies, where the droplet adjusts its shape quickly upon initial contact to minimize the surface energy. It is important to mention, however, that the nandroplet undergoes significant vibration on all the surfaces at 50 ps to 1000 ps, as seen in Fig. 3, 4 and 5. The energy fluctuations and the resultant variability in surface tension at the nanoscale lead to a set of dynamic instabilities [39]. Additionally, intrinsic thermal motion and molecular interactions within the droplet cause continuous vibrations [40]. The higher surface area-to-volume ratio in nanoscale droplets can increase these effects, leading to noticeable oscillations [39, 40].

3.2 Static contact angle of nanodroplet on Ti surfaces

It is important to highlight again that the nanodroplet on flat and rough Ti surfaces begins to reach a stable configuration at about 50 ps as shown in Fig. 3, 4, and 5. Therefore, this time scale is used to calculate the static CAs on the corresponding surfaces. The estimation of the static CAs of water nanodroplets on Ti surfaces enables the measurement of the surface wettability.

The determination of CA at the atomistic scale poses significant challenges since the nanodroplet boundaries undergo continuous changes influenced by molecular interactions, inherent fluctuations, droplet vibrations, shape changes, and surface roughness [41]. It is difficult to precisely define the nanodroplet shape at any specific moment. In the literature, the CA in MD studies is commonly estimated using a technique that relies on fitting the time-averaged density profile of the droplet [22, 42, 43].

The approach adopted in measuring the static CA in this study involves using a circular fitting technique [35] on the liquid-vapor interface of water nanodroplets

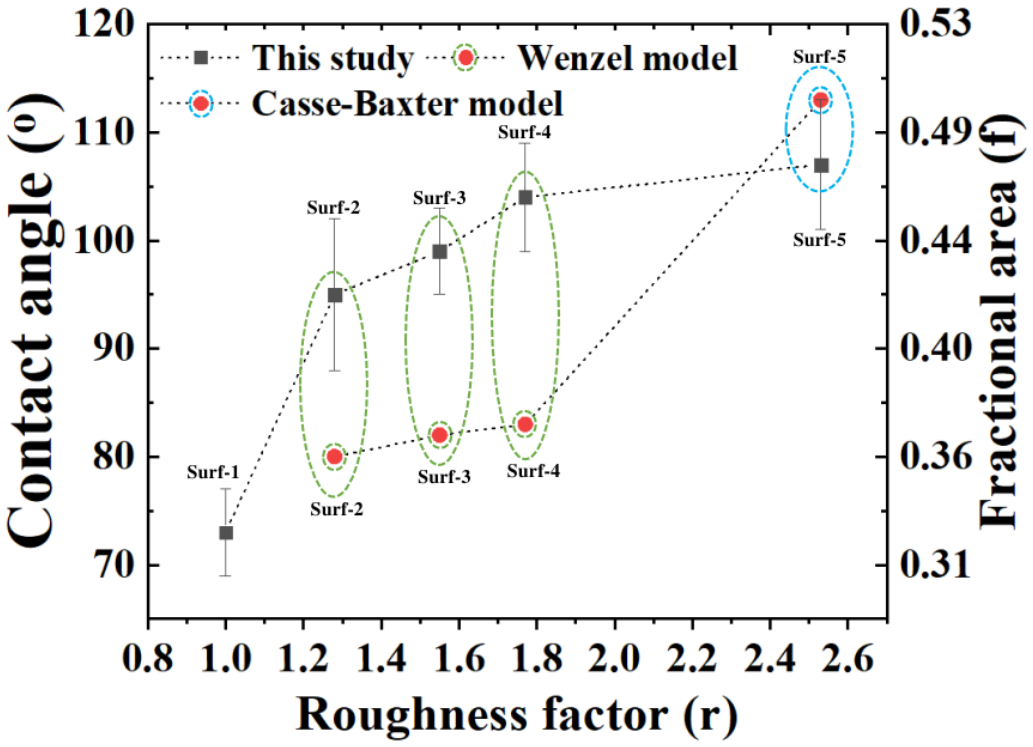

Figure 7: Comparison of Contact Angle (CA) predictions between MD simulations and classical wetting models (Wenzel and Cassie-Baxter) for Ti Surfaces with nanometric reliefs.

on flat Ti surfaces, as illustrated by the density profile plots in Fig. 6 (a) and (b). Hence, Fig. 6 (a) shows the CA of a water nanodroplet on a flat Ti surface, and Fig. 6 (b) shows the density profile of the nanodroplet on the same surface. The density profile was generated by dividing the simulation domain into two-dimensional slices perpendicular to the y-z plane. To draw the density profile, the water density was computed for each slice with a size of 0.2 nm × 0.2 nm.

In the density profile, 1 corresponds to the liquid and 0 corresponds to the vapor. The liquid-vapor boundary was taken at the point where the density is half ($0.5\ g/cm^3$) of the bulk of the water nanodroplet. Both visualizations are used to determine the static CA on flat Ti. The circular fitting was made in such a way that it passes above Ti surface such that near the wall density points of the droplet is omitted to avoid the influence from vibration at the liquid-solid interface [26]. The water CA was then determined using commercially available software [44] to calculate the angle formed between the tangent line at the contact point on the liquid-vapor interface and the Ti surface.

A series of 20 snapshots were taken at time intervals of 50 ps. Taking this large number of snapshots at different points in the simulation allows us to average out the random fluctuations and obtain a more reliable estimate of the average CA. As such, the final static water CA was determined by averaging the measured values and accounting for the associated error. The snapshots of the CA calculation on flat Ti are summarized in the Supporting Information (Fig. 1.0). For the flat Ti surface, the estimated CA is $73° \pm 4°$, indicating that the flat Ti surface is strongly hydrophilic. Despite the size of the droplet being considerably smaller than those encountered in the experimental works [45–49], the obtained CA value falls within the range of experimental observations on polished Ti. It is important to note that the CA in experiments can vary depending on the specific surface preparation and cleanliness of the Ti surface. Most of the CA values reported in the experimental literature for untreated Ti are 48.2° [45], 53.2°[46], 56° [47], 66.4° [48] and 75.5° [49]. Consequently, the MD simulations faithfully reproduced the experimentally observed CAs for Ti surfaces, confirming the accuracy and reliability of the computational predictions of CA using an atomistic approach.

In what follows, the static CA for Surf-2, 3, 4, and 5 were estimated using the same procedure. And the corresponding static CAs for these surfaces are $95° \pm 7°$, $99° \pm 4°$, $104° \pm 5°$ and $107° \pm 6°$ respectively. The introduced roughness amplifies the CA of the flat Ti surface from a hydrophilic to a hydrophobic state, consistent with earlier discussed droplet dynamics and trends generally observed in the literature.

3.3 Effect of surface roughness on static contact angle

Following the fact that the introduced roughness on Ti surfaces, Surf-2, 3, 4, and 5 changes the wetting conditions as earlier stated, classic wetting theories such as the Wenzel and Cassie-Baxter theories are used to predict the CA on the surfaces. The results are then compared with the MD numerical simulation to study the effect of the surface roughness on static CA on Ti surfaces. More details on the classical theories can be

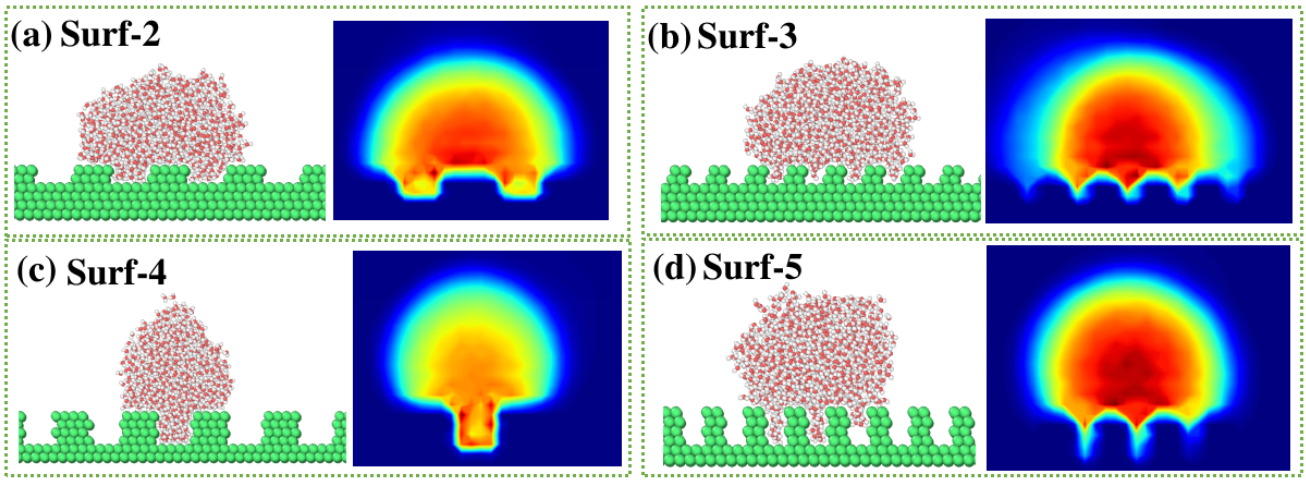

Figure 8: Snapshots of the equilibrium state and density profile of water nanodroplets on various Ti surfaces with different nanometric surface reliefs.

found in the "Supporting Information 1.2".

Fig. 7 shows the comparison of MD simulations in this study with those predicted by classical wetting models, specifically the Wenzel and Cassie-Baxter models, for Ti with nanometric surface reliefs. The flat Ti surface (Surf-1) serves as a baseline for understanding the wetting behavior without any influence of roughness. The CA observed in the MD simulations for this surface is close to the intrinsic Young contact angle. This value sets the stage for comparing how roughness modifies the wettability of the surface.

The MD simulations show an increase in the static CA for Surf-2, 3, and 4 compared to the flat surface (Surf-1). This behavior shows that the droplet conforms to the surface roughness, increasing the actual contact area between the nanodroplet and the nanorough Ti surface. As a result of this, the wetting properties of the surfaces changed from a hydrophilic state to a hydrophobic state. The Wenzel model also predicted a higher CA compared to the flat surface, thus confirming the effect of the introduced relief. However, there is a disagreement between the MD calculations and the Wenzel model, as the measured CA in MD is greater than the CA predicted by the Wenzel model, with an observed deviation of about 15°, 17° and 21°. Even though Surf-2, 3, and 4 do not entirely agree with the quantitative predictions of the Wenzel model, the qualitative assumptions of the model can still apply when the droplet fills the textured surfaces and no air pockets are present.

As shown earlier for Surf-5, the water nanodroplet does not fully penetrate the surface roughness but instead rests on top of it, trapping air pockets underneath, thereby increasing the CA. Therefore, the CA observed in the MD simulations for Surf-5 is higher than that of the other four surfaces. The Cassie-Baxter model predicts an even higher CA than the MD results, indicating partial agreement between the model and the MD simulations. This partial agreement suggests that Surf-5 exhibits characteristics of the Cassie-Baxter regime, where the reduced solid-liquid contact area results in an increased CA and amplified hydrophobic effect.

To better confirm the wetting regime of the Ti surfaces described above, we compared the equilibrium state of the nanodroplet and the density profile plot, as shown in Fig. 8. This comparison provides a clear visualization of how the nanodroplet interacts with the various surface textures. Surf-2 and 4 exhibit a fully wetted state, indicating that the droplets adapt to the shape and contours of the surface roughness. In addition, Surf-2, for instance, fills two of the surface grooves, resulting in a lower CA compared to Surf-4. Surf-4, although filling only one groove, shows a higher CA than Surf-2. This behavior supports the Wenzel regime, where the droplet's CA is influenced by the increased surface area due to the roughness.

In the case of Surf-3 and 5, the wetting trends are similar but distinct from Surf-2 and 4. On Surf-3, the water droplet fully occupies the grooves of the surface textures, consistent with what is observed in the Wenzel wetting regime. Surf-5, however, demonstrates a different interaction. The nanodroplet in Surf-5 partially fills the grooves, similar to Surf-3, but leaves portions of the relief empty, creating air pockets beneath the droplet. This partial filling and presence of air pockets lead to a higher CA, consistent with the Cassie-Baxter regime.

Therefore, Surf-5 represents the Cassie-Baxter state, where the surface roughness promotes the formation of a bi-phase air-liquid layer at the interface thus increasing hydrophobicity. On the other hand, Surf-2, 3, and 4 exhibit characteristics of the Wenzel state, where the droplet fully wets the rough surface, leading to different degrees of wettability as indicated by their CAs. This analysis further confirms the claim in the dynamic and spreading process of water nanodroplet on different Ti surfaces.

Fig. 9 illustrates the relationship between the water-solid interaction energy and the roughness factor (r) of Ti surfaces. This interaction energy, defined as the total van der Waals interaction between water

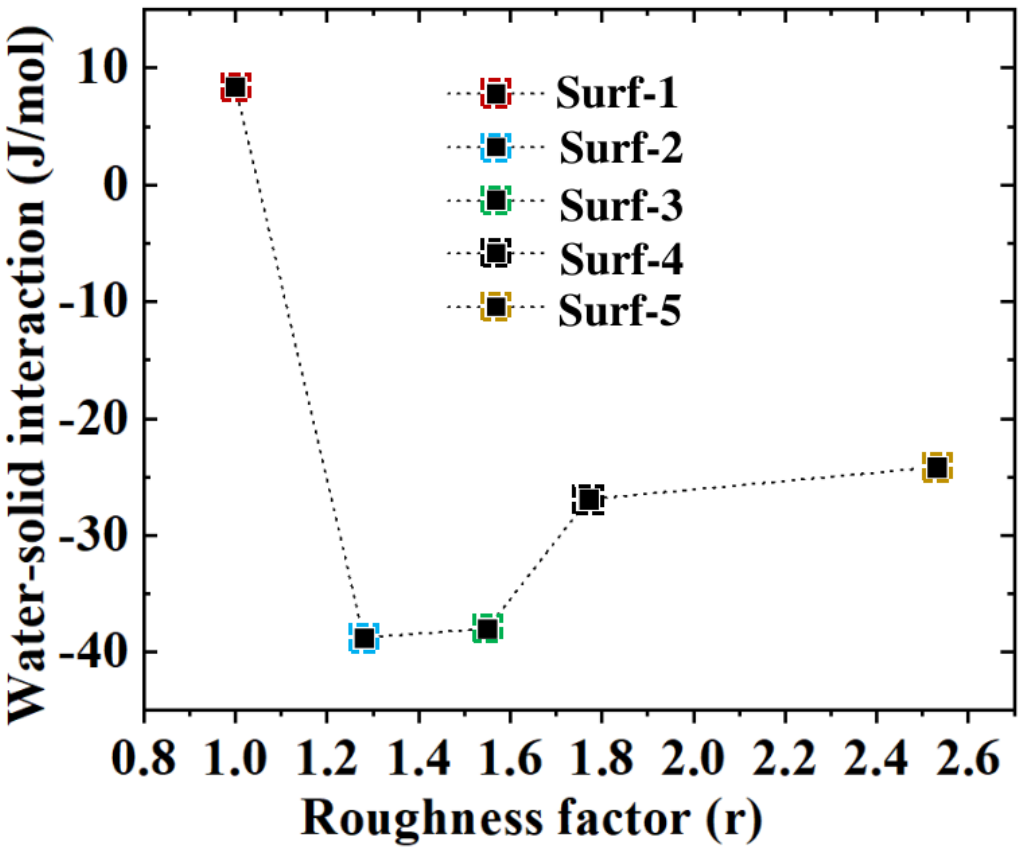

Figure 9: Water-solid interaction energy for flat and rough Ti surfaces with different roughness factors (r).

molecules and Ti surfaces is important in understanding the behavior of nanodroplet in contact with varying surface roughness on Ti. For the flat surface (Surf-1), the interaction energy is positive, which indicates a net repulsive force between water molecules and the flat Ti surface leading to weaker adhesion properties with nanodroplet due to smaller surface area for interaction.

In Surf-2, the interaction energy is negative. This sharp drop reveals strong adhesive interactions, which lead to wetting of the rough Ti surface by the nanodroplet. This phenomenon is due to the increased surface area and roughness that increased the Van der Waals interactions between the water molecules and the rough Ti surface. This further gives more validation to why the spreading radius of Surf-2 is significantly higher than the other surfaces as previously discussed. Surf-3 shows a slight reduction in the magnitude of interaction energy. This demonstrates that the highly attractive interactions noted in Surf-2 are slightly reduced as roughness continues to increase.

In Surf-4, the interaction energy becomes less negative, indicating weaker interactions. This trend continues with Surf-5, where the interaction energy is even less negative compared to Surf-4. This demonstrates weaker interactions, leading to non-wetting behavior. These observations show that as the roughness increases, the attractive interactions between the nanodroplet and the Ti surface diminish, making the surface more hydrophobic. This occurs because the nanodroplet does not fully conform to the rough surface, resulting in fewer contact points for Van der Waals interactions. Further increasing the roughness reduces the magnitude of these attractive forces. This finding is consistent with trends in the literature, which show that when the droplet state transitions from the Wenzel state to the Cassie state, the interaction energy decreases sharply [32, 33]. Therefore, understanding and controlling surface roughness can play an important role in tailoring the interfacial properties of Ti surfaces for specific applications. Future research could focus on a deeper investigation of the transition points between different wetting states for a more comprehensive understanding.

4 Conclusions

MD simulations have been used to investigate the wetting behaviors of a water nanodroplet on flat and structured Ti solid surfaces with different roughness scales. Four different roughness scales have been considered to study both static and dynamic wetting phenomena of water nanodroplets on Ti surface. The static contact angle obtained for the flat Ti surface agrees with the experimental observation. Additionally, a lower spreading radius of water nanodroplets has been observed on Ti surfaces with a high roughness scale compared to other rough surfaces showing the direct correlation between the roughness and the spreading behavior. The spreading process is affected by the ratio of the structure period to the nanodroplet diameter, especially when these values are comparable. The results

of the dynamic contact angle of water nanodroplets on the flat Ti surface and those of the rough surfaces showed a gradual decrease over time, illustrating an evolution toward a hydrophobic state. The degree of roughness and the specific dimensions of the surface grooves determine these wetting processes. Surfaces with larger grooves and spacing tend to support more extensive spreading, while those with narrower grooves and higher roughness limit spreading. Our MD simulations further validate this claim even when their results deviate from the data given by the available phenomenological models. It should be noticed that the decrease in the interaction energy facilitates transitions from the Wenzel state to the Cassie state. Overall, we believe that these simulations have improved our understanding of how Ti surface relief can be designed for many applications, in particular for anti-viral surface treatment and other biomedical applications.

Declaration of competing interest

The authors declare no conflicts of interest.

Acknowledgments

The research was funded by the French Ministère de l'Éducation Nationale and the FET Laser Implant project, which is part of the EU HORIZON 2020 program, under Grant Agreement ID: 951730. We wish to acknowledge the support provided in part by EUR Manutech Sleight and Labex Manutech-SISE. We extend our gratitude for the computational support provided by Hubert Curien Laboratory and CINES, France, referenced under project number AD010814604R1.

References

[1] C. Elias, J. Lima, R. Valiev, and M. Meyers, Biomedical applications of titanium and its alloys, *Jom* **60**, 46 (2008).

[2] S. Kligman, Z. Ren, C.-H. Chung, M. A. Perillo, Y.-C. Chang, H. Koo, Z. Zheng, and C. Li, The impact of dental implant surface modifications on osseointegration and biofilm formation, *Journal of clinical medicine* **10**, 1641 (2021).

[3] A. Y. Vorobyev and C. Guo, Direct femtosecond laser surface nano/microstructuring and its applications, *Laser & Photonics Reviews* **7**, 385 (2013).

[4] J. Yong, F. Chen, Q. Yang, Z. Jiang, and X. Hou, Hall of fame article: A review of femtosecond-laser-induced underwater superoleophobic surfaces (adv. mater. interfaces 7/2018), *Advanced Materials Interfaces* **5**, 1870033 (2018).

[5] K. Sugioka and Y. Cheng, Ultrafast lasers—reliable tools for advanced materials processing, *Light: Science & Applications* **3**, e149 (2014).

[6] R. A. Gittens, L. Scheideler, F. Rupp, S. L. Hyzy, J. Geis-Gerstorfer, Z. Schwartz, and B. D. Boyan, A review on the wettability of dental implant surfaces ii: Biological and clinical aspects, *Acta biomaterialia* **10**, 2907 (2014).

[7] D. Quéré, Wetting and roughness, *Annu. Rev. Mater. Res.* **38**, 71 (2008).

[8] B. Wu, M. Zhou, J. Li, X. Ye, G. Li, and L. Cai, Superhydrophobic surfaces fabricated by microstructuring of stainless steel using a femtosecond laser, *Applied surface science* **256**, 61 (2009).

[9] A. Cunha, A. P. Serro, V. Oliveira, A. Almeida, R. Vilar, and M.-C. Durrieu, Wetting behaviour of femtosecond laser textured ti–6al–4v surfaces, *Applied Surface Science* **265**, 688 (2013).

[10] O. Raimbault, S. Benayoun, K. Anselme, C. Mauclair, T. Bourgade, A.-M. Kietzig, P.-L. Girard-Lauriault, S. Valette, and C. Donnet, The effects of femtosecond laser-textured ti-6al-4v on wettability and cell response, *Materials Science and Engineering: C* **69**, 311 (2016).

[11] H.-q. Dou, H. Liu, S. Xu, Y. Chen, X. Miao, H. Lü, and X. Jiang, Influence of laser fluences and scan speeds on the morphologies and wetting properties of titanium alloy, *Optik* **224**, 165443 (2020).

[12] R. N. Wenzel, Resistance of solid surfaces to wetting by water, *Industrial & engineering chemistry* **28**, 988 (1936).

[13] A. Cassie and S. Baxter, Wettability of porous surfaces, *Transactions of the Faraday society* **40**, 546 (1944).

[14] P. Bizi-Bandoki, S. Benayoun, S. Valette, B. Beaugiraud, and E. Audouard, Modifications of roughness and wettability properties of metals induced by femtosecond laser treatment, *Applied Surface Science* **257**, 5213 (2011).

[15] Y. Zhang, Y. Jiao, C. Li, C. Chen, J. Li, Y. Hu, D. Wu, and J. Chu, Bioinspired micro/nanostructured surfaces prepared by femtosecond laser direct writing for multi-functional applications, *International Journal of Extreme Manufacturing* **2**, 032002 (2020).

[16] J. H. Park and N. Aluru, Temperature-dependent wettability on a titanium dioxide surface, *Molecular Simulation* **35**, 31 (2009).

[17] B. Ohler and W. Langel, Molecular dynamics simulations on the interface between titanium dioxide and water droplets: A new model for the contact angle, *The Journal of Physical Chemistry C* **113**, 10189 (2009).

[18] P. Zhu, D. Dastan, L. Liu, L. Wu, Z. Shi, Q.-Q. Chu, F. Altaf, and M. K. Mohammed, Surface wettability of various phases of titania thin films: Atomic-scale simulation studies, *Journal of Molecular Graphics and Modelling* **118**, 108335 (2023).

[19] I. S. Omeje and T. E. Itina, Numerical study of the wetting dynamics of droplet on laser textured surfaces: Beyond classical wenzel and cassie-baxter model, *Applied Surface Science Advances* **9**, 100250 (2022).

[20] I. S. Omeje, J. Prada-Rodrigo, E. Gamet, Y. Di Maio, R. Guillemet, T. Itina, and X. Sedao, Prediction of wetting behaviours of femtosecond laser texturized surfaces, *Journal of Laser Mi-*

cro/Nanoengineering **00**, 0 (2024).

[21] H. J. Berendsen, J. R. Grigera, and T. P. Straatsma, The missing term in effective pair potentials, *Journal of Physical Chemistry* **91**, 6269 (1987).

[22] L. Chen, S.-Y. Wang, X. Xiang, and W.-Q. Tao, Mechanism of surface nanostructure changing wettability: A molecular dynamics simulation, *Computational Materials Science* **171**, 109223 (2020).

[23] J.-P. Ryckaert, G. Ciccotti, and H. J. Berendsen, Numerical integration of the cartesian equations of motion of a system with constraints: molecular dynamics of n-alkanes, *Journal of computational physics* **23**, 327 (1977).

[24] R. W. Hockney and J. W. Eastwood, *Computer simulation using particles* (crc Press, 2021).

[25] T. Darden, D. York, and L. Pedersen, Particle mesh ewald: An n·log(n) method for ewald sums in large systems, *The Journal of Chemical Physics* **98**, 10089 (1993).

[26] M. Barisik and A. Beskok, Wetting characterisation of silicon (1, 0, 0) surface, *Molecular Simulation* **39**, 700 (2013).

[27] M. P. Allen, D. J. Tildesley, et al., Computer simulation of liquids, *Clarendon-0.12* (1987).

[28] M. P. Allen and D. J. Tildesley, *Computer simulation of liquids* (Oxford university press, 2017).

[29] B. Guillot, A reappraisal of what we have learnt during three decades of computer simulations on water, *Journal of molecular liquids* **101**, 219 (2002).

[30] F. Song, B. Li, and C. Liu, Molecular dynamics simulation of nanosized water droplet spreading in an electric field, *Langmuir* **29**, 4266 (2013).

[31] A. Narten and H. Levy, Liquid water: Molecular correlation functions from x-ray diffraction, *The Journal of Chemical Physics* **55**, 2263 (1971).

[32] D. Niu and G. Tang, Static and dynamic behavior of water droplet on solid surfaces with pillar-type nanostructures from molecular dynamics simulation, *International Journal of Heat and Mass Transfer* **79**, 647 (2014).

[33] J. Zhao, B. Wang, Y. Pan, W. Wang, and C. Zhao, Molecular dynamics simulation on wetting behaviors of n-octane and water droplets on polytetrafluoroethylene surfaces, *Chemical Physics Letters* **785**, 139161 (2021).

[34] D. Frenkel and B. Smit, *Understanding molecular simulation: from algorithms to applications* (Elsevier, 2023).

[35] H. Yaghoubi and M. Foroutan, Molecular investigation of the wettability of rough surfaces using molecular dynamics simulation, *Physical Chemistry Chemical Physics* **20**, 22308 (2018).

[36] T. Koishi, K. Yasuoka, S. Fujikawa, T. Ebisuzaki, and X. C. Zeng, Coexistence and transition between cassie and wenzel state on pillared hydrophobic surface, *Proceedings of the National Academy of Sciences* **106**, 8435 (2009).

[37] S. Plimpton, Fast parallel algorithms for short-range molecular dynamics, *Journal of computational physics* **117**, 1 (1995).

[38] A. Stukowski, Visualization and analysis of atomistic simulation data with ovito–the open visualization tool, *Modelling and simulation in materials science and engineering* **18**, 015012 (2009).

[39] J. G. Sampayo, A. Malijevskỳ, E. A. Müller, E. de Miguel, and G. Jackson, Communications: Evidence for the role of fluctuations in the thermodynamics of nanoscale drops and the implications in computations of the surface tension, *The Journal of chemical physics* **132** (2010).

[40] A. Malijevskỳ and G. Jackson, A perspective on the interfacial properties of nanoscopic liquid drops, *Journal of Physics: Condensed Matter* **24**, 464121 (2012).

[41] E. E. Santiso, C. Herdes, and E. A. Müller, On the calculation of solid-fluid contact angles from molecular dynamics, *Entropy* **15**, 3734 (2013).

[42] R. Šolc, M. H. Gerzabek, H. Lischka, and D. Tunega, Wettability of kaolinite (001) surfaces—molecular dynamic study, *Geoderma* **169**, 47 (2011).

[43] S. Do Hong, M. Y. Ha, and S. Balachandar, Static and dynamic contact angles of water droplet on a solid surface using molecular dynamics simulation, *Journal of colloid and interface science* **339**, 187 (2009).

[44] C. A. Schneider, W. S. Rasband, and K. W. Eliceiri, Nih image to imagej: 25 years of image analysis, *Nature methods* **9**, 671 (2012).

[45] A. Cunha, A.-M. Elie, L. Plawinski, A. P. Serro, A. M. B. do Rego, A. Almeida, M. C. Urdaci, M.-C. Durrieu, and R. Vilar, Femtosecond laser surface texturing of titanium as a method to reduce the adhesion of staphylococcus aureus and biofilm formation, *Applied Surface Science* **360**, 485 (2016).

[46] H.-S. Kim, M.-K. Ji, W.-H. Jang, K. Alam, H.-S. Kim, H.-S. Cho, and H.-P. Lim, Biological effects of the novel mulberry surface characterized by micro/nanopores and plasma-based graphene oxide deposition on titanium, *International Journal of Nanomedicine* 7307–7317 (2021).

[47] C.-F. Liu, T.-H. Lee, J.-F. Liu, W.-T. Hou, S.-J. Li, Y.-L. Hao, H. Pan, and H.-H. Huang, A unique hybrid-structured surface produced by rapid electrochemical anodization enhances biocorrosion resistance and bone cell responses of β-type ti-24nb-4zr-8sn alloy, *Scientific reports* **8**, 6623 (2018).

[48] A. T. Rad, M. Solati-Hashjin, N. A. A. Osman, and S. Faghihi, Improved bio-physical performance of hydroxyapatite coatings obtained by electrophoretic deposition at dynamic voltage, *Ceramics International* **40**, 12681 (2014).

[49] S. Goodarzi, F. Moztarzadeh, N. Nezafati, and H. Omidvar, Titanium dioxide nanotube arrays:

A novel approach into periodontal tissue regeneration on the surface of titanium implants, *Advanced Materials Letters* **7**, 209 (2016).